

# Measuring scattering light distributions on high-absorptive surfaces for stray-light reduction in gravitational-wave detectors

SIMON ZEIDLER, TOMOTADA AKUTSU, YASUO TORII, YOICHI ASO

<sup>1</sup>*Gravitational Wave Project, National Astronomical Observatory of Japan, 2-21-1 Osawa, Mitaka, Tokyo 181-8588, Japan*

<sup>2</sup>*ICRR, The University of Tokyo, 5-1-5 Kashiwa-no-Ha, Kashiwa City, Chiba, 277-8582, Japan*  
*\*simon.zeidler@nao.ac.jp*

**Abstract:** In order to establish scattering measurements in material investigations for gravitational-wave detectors, we have built-up devices for measuring the hemispherical scattering distribution of materials which are planned to be used in those detectors as suppressors of scattered light. The measurement benches we have built, a hemispherical goniometer and a direct back-scatterometer, have a maximum background noise of  $\sim 10^{-4} \text{sr}^{-1}$  BRDF at  $1.064 \mu\text{m}$  wavelength which is the wavelength of the laser-light for our large interferometer for detecting gravitational waves, KAGRA. With these instruments, we have characterized the surface scattering of, e.g., NiP platings, metals, and different carbonaceous coatings, which are supposed to minimize the amount of scattered light in interferometers. The three most important materials for KAGRA's construction (SiC, "Solblack", and "VantaBlack") are presented in this paper. Furthermore, we will try to explain the scattering distributions with the generalized Harvey-Shack model (smooth-surface approximation) which is a common method for surface-scattering calculations. At the end, we give also some valuations about the vacuum compatibility of the materials, which is important for instruments like KAGRA that work under ultra-high vacuum conditions.

© 2019 Optical Society of America

*Keywords:*

---

## References and links

1. N. S. Goel, I. Rohzenal, and R. L. Thompsen, "A computer graphics based model for scattering from objects of arbitrary shapes in the optical region," *Remote Sens. Environ.* pp. 73–104 (1991).
2. B. Sun, R. Ramamoorthi, S. G. Narasimhan, and S. K. Nayar, "A practical analytic single scattering model for real time rendering," *ACM Transactions on Graphics* pp. 1040–1049 (2005).
3. J. E. Harvey, N. Choi, A. Krywonos, S. Schröder, and D. H. Penalver, "Scattering from moderately rough interfaces between two arbitrary media," *Proc. SPIE* **7794**, 77940 (2010).
4. A. Krywonos, "Predicting surface scatter using a linear systems formulation of non-paraxial scalar diffraction," Ph.D. thesis (2000).
5. S. Schröder, T. Herffurth, H. Blaschke, and A. Duparre, "Angle-resolved scattering: an effective method for characterizing thin-film coatings," *Appl. Opt.* **50**, 164–171 (2010).
6. A. Krywonos, J. E. Harvey, and N. Choi, "Linear systems formulation of scattering theory for rough surface with arbitrary incident and scattering angles," *J. Opt. Soc. Am. A*, **28**, 1121–1139 (2011).
7. S. Zeidler, T. Akutsu, Y. Torii, E. Hirose, Y. Aso, and R. Flaminio, "Calculation method for light scattering caused by multilayer coated mirrors in gravitational wave detectors," *Opt. Express* **25**, 4741–4760 (2017).
8. E. Theocharous, C. J. Chunnillall, R. Mole, D. Gibbs, N. Fox, N. Shang, G. Howlett, B. Jensen, R. Taylor, J. R. Reveles, O. B. Harris, Ahmed, and Naseer, "The partial space qualification of a vertically aligned carbon nanotube coating on aluminium substrates for eo applications," *Opt. Express* **22**, 1–18 (2013).
9. T. Akutsu, Y. Saito, Y. Sakakibara, Y. Sato, Y. Niwa, N. Kimura, T. Suzuki, K. Yamamoto, C. Tokoku, S. Koike, D. Chen, S. Zeidler, K. Ikeyama, and Y. Ariyama, "Vacuum and cryogenic compatible black surface for large optical baffles in advanced gravitational-wave telescopes," *Opt. Mater. Express* **6**, 1–14 (2016).
10. D. Riley and M. Smith, "Controlling light scatter in advanced ligo," *Tech. Rep. T080064-00-D*, LIGO Scientific Collaboration (2008).
11. H. Abderrazak and E. S. B. H. Hmida, "Silicon carbide: Synthesis and properties," in *Properties and Applications of Silicon Carbide*, R. Gerhardt, ed. (InTech, 2011).
12. S. Zeidler, T. Posch, H. Mutschke, H. Richter, and O. Wehrhan, "Near-infrared absorption properties of oxygen-rich stardust analogs - the influence of coloring metal ions," *A&A* **526**, A68 (2011).

13. J. A. Dillon, R. E. Schlier, and H. E. Farnsworth, "Some surface properties of silicon-carbide crystals," *J. Appl. Phys.* **30**, 675–679 (1958).
14. G. Volkova, O. Doroshkevych, A. Shylo, T. Zelenyak, V. Burkhovetskiy, I. Danilenko, and T. Konstantinova, "Structural evolution of silicon carbide nanopowders during the sintering process," *J. Ceram.* **2014**, 723627 (2014).
15. J. E. Harvey, S. Schröder, N. Choi, and A. Duparre, "Total integrated scatter from surfaces with arbitrary roughness, correlation widths, and incident angles," *Opt. Eng.* **51**, 013402 (2012).
16. D. Beckett, Y. Liu, and D. Hawthorne, "Investigation of the blackening process of electroless nickel-phosphorous coatings and their properties," *Products Finishing* (2011). Online article.
17. R. Parkinson, "Properties and applications of electroless nickel," *Nickel Development Institute Technical Series* pp. 1–33 (1997).
18. J. Lehman, C. Yung, N. Tomlin, D. Conklin, and M. Stephens, "Carbon nanotube-based black coatings," *Appl. Phys. Rev.*, Volume 5, Issue 1, id.011103 **5**, 011103 (2018).
19. G. T. Georgiev and J. J. Butler, "Laboratory-based bidirectional reflectance distribution functions of radiometric tarps," *Appl. Opt.* **47**, 3313–3323 (2008).
20. E. L. Church and P. Z. Takacs, "The optimal estimation of finish parameters," *Proc. SPIE* **1530**, 71–86 (1991).
21. H. W. Jensen, S. R. Marschner, M. Levoy, and P. Hanrahan, "A practical model for subsurface light transport," *ACM SIGGRAPH* pp. 511–518 (2001).
22. W. H. Peake and D. E. Barrick, "Scattering from surfaces with different roughness scales; analysis and interpretation," *Electroscience laboratory, The Ohio State University, Columbus, Ohio 43212* (1967).
23. L. Tsang and J. A. Kong, *Scattering of electromagnetic waves - advanced topics*, (John Wiley and Sons, 2001).
24. S. Alleg, A. Boussaha, W. Tebib, M. Zergoug, and J. J. Sunol, "Microstructure and magnetic properties of nip alloys," *J. Supercond. Nov. Magn.* **29**, 1001–1011 (2016).
25. E. Dumont, B. Dugnoille, J. Petitjean, and M. Barigand, "Optical properties of nickel thin films deposited by electroless plating," *Thin Solid Films* **301**, 149–153 (1997).
26. X. Wu, L. Pan, H. Li, X. Fan, T. Yong Ng, D. Xu, and C. Zhang, "Optical properties of aligned carbon nanotubes," *Phys. Rev. B*, vol. 68, Issue 19, id. 193401 **68**, 193401 (2003).
27. F. J. Garcia-Vidal, J. M. Pitarke, and J. B. Pendry, "Effective medium theory of the optical properties of aligned carbon nanotubes," *Phys. Rev. Lett.* **78**, 4289–4292 (1997).
28. K. Lipert, M. Ritschel, A. Leonhardt, Y. Krupskaya, B. Buechner, and R. Klingeler, "Magnetic properties of carbon nanotubes with and without catalyst," *J. Phys.: Conf. Ser.* **200**, 072061 (2010).

## 1. Introduction

Many applications in the wide field of optics and material science are focused on the influence of surfaces on the propagation of light. Moreover, to know the spatial distribution of either reflected or transmitted light has become very important also in 3-D computer-graphics design (see for instance [1, 2]). In particular, constraints for modern high-precision optical systems become tighter and tighter. A popular example are interferometric gravitational-wave detectors like LIGO in the USA, VIRGO in Italy, and KAGRA in Japan, and their future generations. Light scattering is already an important issue for such instruments and it is reasonable to assume that in the future the influence of scattering will become an even bigger problem. The first step to take measures against these problems is a proper understanding of the scattering from the optical components in such systems.

Usually, vector perturbation methods like those from Rayleigh-Rice (RR) or scalar methods like the General Harvey-Shack (GHS) theory are used [3, 4] to model the expected angular distribution of scattered light. However, all these models rely on input data which have to be determined by measurements, especially the surface power-spectral density (PSD), and have restricted application ranges. Note that the absolute values of the spatial frequency from which the PSD is a function need to be smaller than  $1/\lambda$  for the models to be valid [3]. Therefore, direct measurements of the scattering especially at wide scattering angles are still important. Also, reference data, again to be determined by measurements, are needed to compare the respective model with reality. For surfaces, however, for which no metrology is available or applicable (e.g., surfaces of high-roughness or absorption), an analysis of the theoretical scattering is indeed quite difficult.

In order to get information regarding the scattering also from those materials/surfaces, a direct measurement of the scattering is often unavoidable. These measurements can be done basically

either in an integrating sphere or by a goniometer, providing data either of the whole scattered power or the angular distribution of the scattered light which give complementary information, of course. Integrating spheres are very common and a lot of commercial instruments exist that can provide the integrated scattered power. In contrast, a goniometer that meets our specifications was harder to find (although existing in other institutes, e.g., in LIGO or as presented in [5]) and we decided to upgrade an already existing goniometer at our institute to our needs. Henceforth, when we speak about scatter goniometers, we will use the more handy term scatterometer.

In this paper, we will present results on the performance of our scatterometer and in measuring the scattered light from different samples which are of particular interest in high-sensitivity interferometers. Our goal was not only to get information on the hemispherical distribution of the scattering but also on the directly back-scattered light field, the so called back-scattering. Therefore, in section number two, we will introduce the two devices that we constructed beginning with the device for the hemispherical distribution of scattering light. In section three, we will present measurements on three materials that are promising for the usage as special beam dumps and baffles in the gravitational wave detector KAGRA: silicon carbide (SiC), “Solblack”, and “VantaBlack”, in order to show the usability of these instruments. In addition, in section four, we will compare the measurements with theoretically calculated values to proof their consistency. The paper is closed with a discussion about the actual usability of those materials in gravitational-wave detectors.

## 2. Measurement setup

### 2.1. Spatial distribution of scattering light

When an incoming light field hits a surface, a part of it will be reflected back into the surrounding medium. Except for the specular reflection, in any other direction reflected light is called here scattered light. Its spatial distribution is strongly depending on the specific surface properties which are usually treated statistically with the aid of the PSD of this surface. Theories on how to calculate this distribution according to the PSD can be found in the literature [3, 6, 7].

As mentioned already, our goal was to construct a device that can measure the spatial distribution of scattering light in an angular field as wide as possible. A sketch of our instrument is shown in Fig. 1. We are using a photodiode (PD), that rotates within  $-90^\circ$  and  $90^\circ$  latitude around the impact-point of the incoming light-field on a sample’s surface. Additionally, the sample’s orientation in space can be changed on two axes: full rotation around the mounting axis of the optical table, where the whole device is installed and  $\sim 10^\circ$  rotation around the axis perpendicular to the mounting axis and the sample’s surface-normal. However, since the second rotation can be done only with very small accuracy, we used this possibility just for a fine-adjustment of the surface orientation and fixed the axis during a measurement. With this setup it is possible to do hemispherical scattering measurements for any angle-of-incidence (AOI) along the plane-of-incidence.

The light source is provided by a 16 mW fiber laser at  $1.064 \mu\text{m}$  wavelength which is guided through a  $\lambda/4$  and a  $\lambda/2$  plate, followed by a polarizing beam-splitter and another  $\lambda/2$  plate, to control the alignment of the (linear) polarized light and its power. The Gaussian beam is subsequently focused by a lens ( $f=200 \text{ mm}$ ) to reach a diameter of  $\sim 0.5 \text{ mm}$  at the point of impact on the sample. Focusing the beam is important to maintain a considerably high angular resolution also around the specular direction which is important for some of our measurements. The chosen lens focuses the beam in a balanced way, so that we have a reasonably small impact area but the surface of our samples does not get harmed by the laser’s intensity ( $\sim 0.08 \text{ W/mm}^2$ ). The power of the laser has been measured with a separate (calibrated) PD.

The sample-holder itself lies within a triangular shaped chamber with blackened inner walls (see Fig. 1) to avoid influences from scattering light coming from the chamber itself. The laser is chopped in its power amplitude by a lock-in amplifier to which also the PD is connected ( $f_{\text{chopping}} = 190 \text{ Hz}$ ). This excludes the measurement from low-frequency noise sources like

ambient electronic devices and part of the PD's dark-current, which is, without any lock-in amplifier connected, about 2 nA. The current floor-noise of the whole system during a measurement is  $\sim 20$  pA.

The laser reaches the sample through a hole in one of the chamber walls ( $\varnothing 5$  mm). The PD itself is mounted separately on a rotatable arm controlled by a stepping motor ("Oriental Motors Co., Ltd") with at maximum  $0.01^\circ$  precision. The exact number of degrees is set manually with the aid of a control program by "Oriental Motors Co., Ltd" installed on a personal computer. For data taking and saving, the photo-current ( $I_{PC}$ ) measured by the PD is analyzed by a program written in "LabView" on the same computer. Both programs usually run in parallel.

A common form of quantifying the spatial-distributed amount of scattering is the Bidirectional Reflection Distribution Function (BRDF) [3, 6, 7] which may be handled as a kind of generalization of the reflection itself. From  $I_{PC}$  and the distance of PD to impact point on the sample, we can calculate the BRDF via

$$\text{BRDF}_{\text{hsc}} = \frac{I_{PC} \cdot n_{PC}}{P_{\text{laser}} \cdot \Delta\Omega \cdot \cos \theta}. \quad (1)$$

$\Delta\Omega$  is the solid angle from the point of impact towards the surface of the receiver, in our case the PD.  $\theta$  is the scattering latitude relative to the samples normal, toward the receiver. The active surface of the PD has a circular diameter of 1 mm and its distance from the sample is variable from 5 to 10.5 cm. For the calculations the "power-current ratio" or "quantum efficiency" ( $n_{PC}$ ) of the diode is necessary to convert the current into received power. We can confirm that  $n_{PC}$  is a constant value of  $\sim 4$  W/A in the range of power we are dealing with here. We used the same laser as for the measurements to calibrate the PD in a separate setup where we focused the beam on the PD's surface. However, it should be noted that we did not repeat the calibration every time before a measurement in order not to touch the setup.

The specular-reflection beam from the sample's surface may produce additional diffuse light fields inside the chamber when it hits the inner walls. Although they were blackened by a scattering reducing surface ("Fine Shut"), it can only suppress the diffuse light-field down to  $\text{BRDF} \sim 10^{-4} \text{ sr}^{-1}$  (as received by the PD). Therefore, we have placed a beam dump in the reflected beam, consisting of an Aluminum plate covered with "VantaBlack", a coating made of vertical aligned carbon nano-tubes and claimed to be the blackest artificial material on Earth [8]. We took also measurements of this coating regarding its light-scatter properties and will present the results in this paper. The measurement error due to dark-current and other electrical noises can be estimated to be  $\lesssim 7.6 \cdot 10^{-5} / \cos \theta \text{ sr}^{-1} \text{ BRDF}$ .

## 2.2. Measuring back-scattered light

Because of the hemispherical scatterometer's setup, the PD will – if the scattering is measured near the plane of incidence – block the incoming laser when its latitude approaches the AOI. Hence, information about the light that scatters directly back toward the laser cannot be measured with such an instrument.

Yet, for the purpose of analyzing materials regarding their scattering properties in a gravitational wave detector like KAGRA, it is substantial to have information on the light that scatters back directly to its source as this will have the biggest impact on the sensitivity of such detectors [7]. The problem of back-scattering is not trivial. Surfaces having roughnesses that can not be considered as smooth may have an increased scattering back toward the incident light that cannot simply be predicted by hemispherical measurements [9].

Therefore, in order to get information also on the back-scattered light, we have built another device with a fixed PD and a rotatable sample holder (Fig. 2). When the laser hits a sample, the light scattered back toward the incoming beam is guided via a beam splitter to the PD. The back-scattered light can be measured for AOIs between  $-60$  and  $60^\circ$ . The calculation of the BRDF

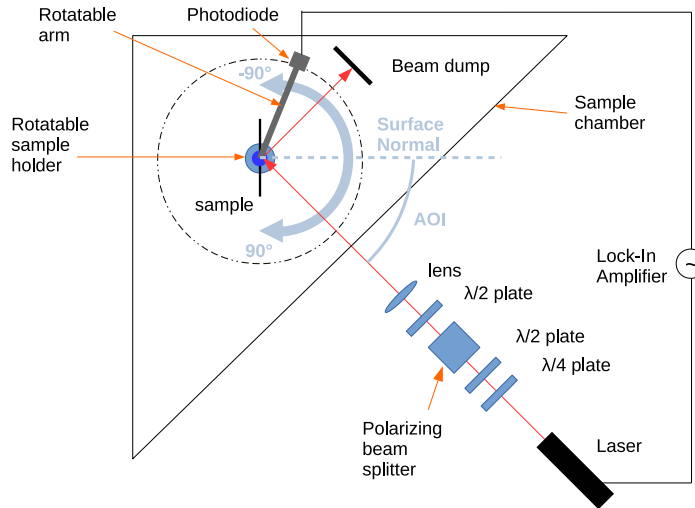


Fig. 1. Sketch of the hemispherical scatterometer and the description of its basic elements. The triangular shape has been chosen to provide additional traps for stray-light and to further reduce the background scattering-noise.

is quite similar to the one given for the scatter-goniometer. We only have to take the beam splitter into account through which both the incident laser and the back-scattered light passes:

$$\text{BRDF}_{\text{bsc}} = \frac{I_{\text{PC}} \cdot n_{\text{PC}}}{P_{\text{laser}}/4 \cdot \Delta\Omega \cdot \cos\theta}. \quad (2)$$

Note that due to the existence of the beam-splitter in front of the sample,  $P_{\text{laser}}/4$  is technically the incident power to the sample. The denomination of the parameters is the same as in Eq. (1). Only, the PD is now approximately 50 cm away from the sample while its circular diameter is the same as for the hemispherical scatterometer.  $n_{\text{PC}}$  is now  $\sim 1.25 \text{ W/A}$  since we used a different PD as for the hemispherical scatterometer. The laser provides a power of 24 mW and is again connected to a lock-in amplifier with the PD. On the sample-surface we find a beam-diameter of  $\sim 1 \text{ mm}$ . Since we use a much smaller solid angle at a fixed position in the scattering hemisphere, we judged a particular focusing not necessary.

As we are using a beam splitter to divide the scattered beam toward laser and detector, the incoming beam is necessarily divided too. In order to avoid it hitting the chamber walls and creating background radiation, we set a light-trap for the unused beam, consisting of an Aluminum cylinder and a KG5 glass window oblique to the beam-direction. Furthermore, the walls of the cylinder are blackened by soot. It is noteworthy that people in LIGO are using a different approach with a mirror having a centered hole for the laser instead of a beam-splitter. However, strictly spoken, they are not measuring the direct back-scattering but small-angle scattering [10].

A drawback of this method, however, is an additional scattering coming from the beam-splitter's coated surfaces when the main beam hits it. This scattered light is very likely to be the main contributor to a diffuse light field inside the measurement chamber that limits the minimum BRDF to be measured. A measurement of this light-field (without any sample and suppressing radiation coming from the sample-chamber by using KG5 windows) resulted in  $\sim 0.0024 / \cos\theta \text{ sr}^{-1}$  BRDF, which has been subtracted from the measurement results to get rid of its influence. However, this

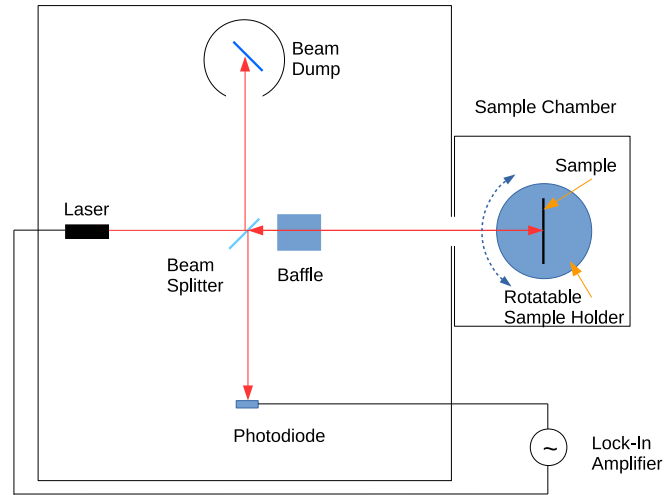


Fig. 2. Sketch of the back-scatterometer and the description of its basic elements. The sample holder is rotatable for changing the AOI. The beam dump in the upper part of the device is one of the key-parts and has been designed as a light-trap.

procedure increases of course the relative error of the measurements especially for small BRDF values. The overall influence of dark-current and other electrical noises can be estimated to be  $\sim 3.71 \cdot 10^{-5} / \cos \theta \text{ sr}^{-1}$  BRDF.

### 3. Results of sample measurements

#### 3.1. SiC

SiC has become quite attractive for the usage in high-temperature environments nowadays because of its high thermal conductivity as well as its extreme chemical and thermal resistivity and hardness. This is especially interesting for damping high-intensity laser radiation. SiC is in its pure form colorless [11] but for a possible usage as a beam-trap in interferometers like KAGRA, it needs to have a high absorptivity in the wavelength of the used laser (usually  $1.064 \mu\text{m}$ ). In practice, the absorption of dielectric materials in near-infrared and visible wavelengths is increased by impurities of metal ions [12]. In case of SiC these are mostly iron or aluminum which give SiC a black-greenish color [13].

We have measured the scattering-light distribution of two samples with different polishing (henceforth called SiC1 and SiC2). Both samples have been provided by the same company and we are thus assuming a similar chemical composition and manufacturing process. As measurements with ZYGO's "NewView8000" metrology instrument show, the surface of both is covered with holes of different diameters (from nm to  $\mu\text{m}$  scale). These holes appear from bubbles filled with gas (see Fig. 3). The reason for the existence of bubbles is the actual manufacturing method of sintering a SiC powder [14], which is often applied for commercial SiC. As can be also seen from the same figure, these holes do not disappear after polishing. In Table 1, the average height distribution, Ra, taken from several different spots on the surface is given for both samples. Assuming a Gaussian height distribution,  $Ra \approx 0.8\sigma_{\text{rms}}$ , where  $\sigma_{\text{rms}}$  is the root-mean-square surface roughness [9, 15], the polishing decreases Ra clearly by a factor of  $\sim 30 - 70$ . The effect

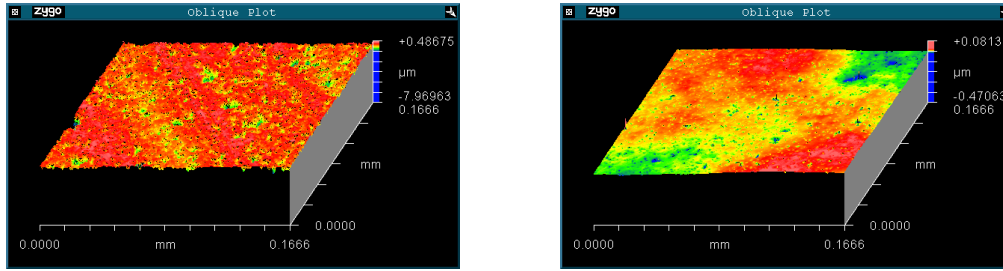


Fig. 3. Image of the surface characteristics of the SiC1 (left) and SiC2 (right) samples taken from the metrology measurements by the “NewView8000” instrument from ZYGO.

is already visible with bare eyes.

Table 1. Table showing the surface parameters that have been obtained with metrology measurements on a Zygo-NewView 8000 instrument.

Parameter	SiC1	SiC2	Solblack (SUS, BA)
Ra (in nm)	145 – 167	2 – 6	130 – 174

Due to the finer polishing, the total integrated scattering [3] is lower for sample SiC2. The compared scattering probabilities of both samples for different AOIs along the plane of incidence (POI) can be seen in Fig. 4. The black circles in the graphs mark the scattering probability according to the back-scattering measurements with unpolarized light. For SiC2, the back-scattering is lower as the hemispherical p-polarization results would suggest but is in a relatively good agreement with the s-polarization curves. Such a distinction cannot be made for the SiC1 sample as the back-scattering value we took at AOI=20°, shows relatively good agreement with the hemispherical scattering measurements in both polarizations. We took data in steps of 1° along the longitude except for the peak around the specular reflection. There, we did the measurements in steps of 0.02° (in an angular range of ±1° around the specular reflection).

The differences between the scattering of the s- and p-polarization for both samples are obviously increasing as the AOI increases. The peak around the specular direction reaches a minimum for p-polarized light, similar to the effect we can expect when approaching the Brewster-angle. Apart from the differences between the peak heights of both samples, there is also a noticeable broad bulge in the scattering distribution for SiC1 around those peak appearing in all AOIs. In this form, the structure is not found for SiC2. Such a broad structure is typical for more roughly polished surfaces and is due to the statistical distribution of the surface height in the spatial-frequency space (this is reflected also in various theories about scattering, for an overview see [4]). For SiC1, it turns out to be the dominant scattering source while for SiC2, just a hint of a bulge may be found at latitudes very close to the specular reflection (within 20 – 30°). For wider angles, however, the scattering seems to be dominated by a Lambertian-like distribution at around 0.001 sr<sup>-1</sup> BRDF, possibly triggered by the holes and very steep structures in the SiC surface.

In a separate setup, we have measured the specular reflectance of both samples by using a photometer with 1 cm diameter, standing approximately 8.3 cm away from the sample, which was mounted on a rotatable holder for realizing different AOIs. The light source was again a 1.064 μm laser. In order to polarize the laser-light into p and s polarization, we used a similar optical setup as for the hemispherical scatter-goniometer. The results of these measurements are shown in Fig. 5. Also, the calculated reflectance from the scattering measurements are shown for all AOIs for which we have taken data (in Fig. 4 the results for only three AOIs are shown). For

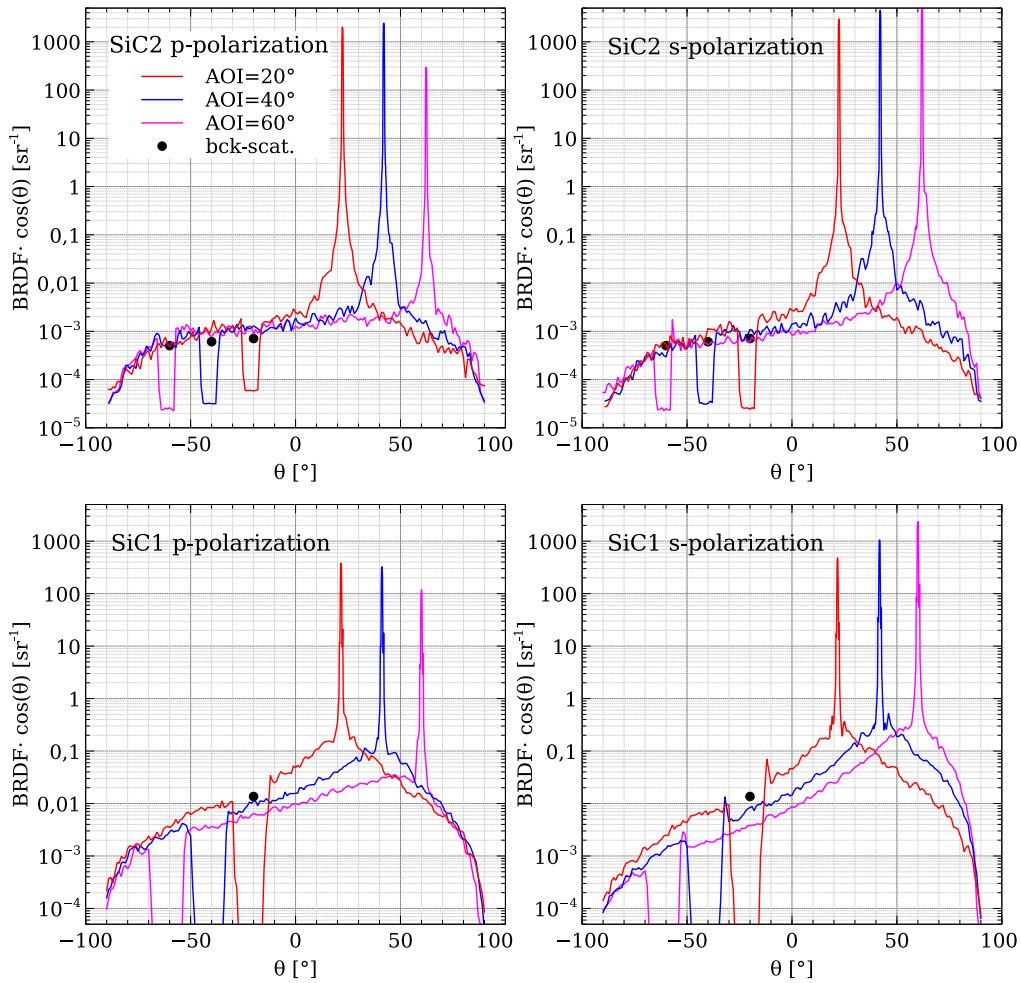


Fig. 4. Comparison of the scattering probabilities along the plane of incidence of the two SiC samples at three different AOIs. The black dots mark the results of the back-scattering measurements at the respective AOI.

the calculations, we assumed a symmetric scattering distribution around the specular peak in all longitudes and latitudes and ran the integration in an angular area around the specular peak which corresponds to the open angle of the photometer used for the reflectance measurements. The results (encircled crosses in the figure) are generally in very good agreement to the measured reflectance. Deviations may be found for wide AOIs in p-polarization, where a factor of  $\sim 1.5 - 2$  difference between measurement and integrated scattering occurred. Some of them may be explainable by the low reflectance due to the Brewster minimum and the corresponding increased measurement error. From the measurements we found such a minimum for the low-polished sample, at around  $65^\circ$  AOI and for the high-polished sample at around  $68^\circ$  AOI (see Fig. 5). A fit-function according to the Fresnel equations has been derived from the measured reflectance data for SiC2. The result of the fit is drawn in the respective graph with a solid line. The derived complex index of refraction is  $2.52 + 0.14i$ . For SiC1, no suitable fit could be found as apparently the stronger scattering weakens the specular reflection too much (compare particularly the reflectance values at  $10^\circ$  AOI between both samples).

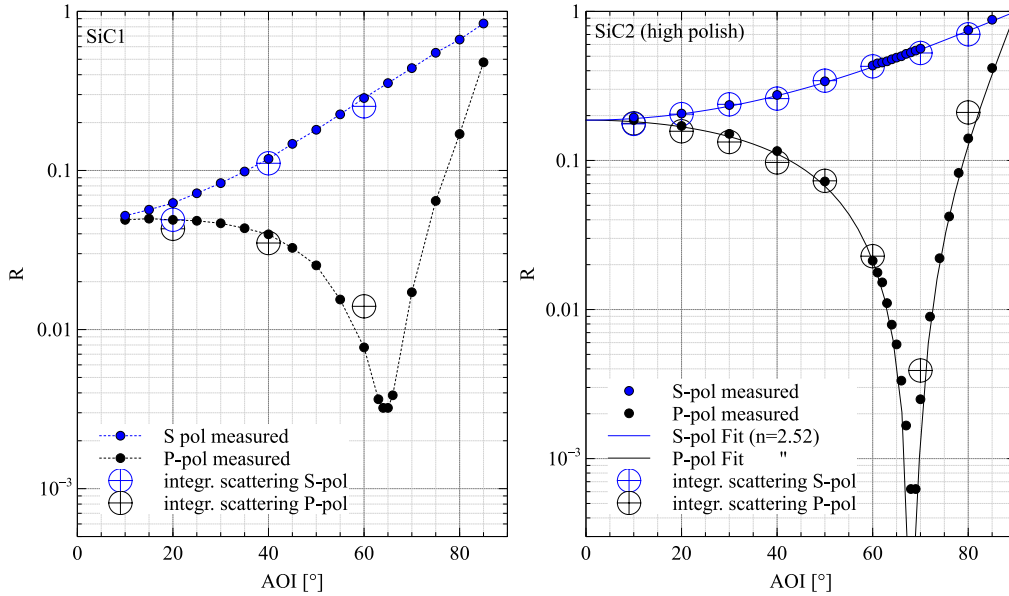


Fig. 5. Results of the reflectance measurements on both SiC samples and the comparison with the integrated scattering around the specular peak.

### 3.2. “Solblack”

Electroless nickel-phosphorus (NiP) plating with subsequent oxidization is a long-established and useful technique for making black surfaces [9, 16]. The NiP plating is featured by its robustness against mechanical and chemical attacks while being comparably thin ( $\sim 10\mu\text{m}$ ), and has a broad application in industries [17]. In KAGRA’s case, a nickel-phosphorus-tungsten (NiPW) plating is used for the black coatings of baffles [9]. The so called “Solblack” coating is manufactured by the Asahi Precision© company and fulfills the main requirements for being used under the conditions of a cryo-cooled vacuum laser-interferometer (sustainability against low temperatures, low outgassing rate, etc.). Solblack is generally high absorbing but also relatively uniform in scattering [9].

That is because of micro-fine fractal structures (a few  $\mu\text{m}$  deep) on the surface [9, 16, 18] which give reason for a Lambertian scattering distribution as it appeared also for the SiC samples (actually, NiP plating does show also on a larger scale a high porosity [18]). Metrology measurements show indeed a lot of jagged structures in a micrometer and sub-micrometer height-range as can be seen in Fig. 7. The roughness as measured with Zygo’s NewView instrument is on a similar level as for the SiC1 sample (see Table 1) and is in total agreement with previous works [9].

Here, we are using the same sample of Solblack that has been used also for the analysis in [9], there indicated as “SUS, BA” meaning that it is Solblack on a stainless steel plate (SUS304 in Japanese Industrial Standard, JIS) for which the surface has been bright-annealed. The steel plate underneath the Solblack coating is very smooth ( $R_a \approx 13 - 17\mu\text{m}$ ) and the wide-angle scattering is less Lambertian than for Solblack on standard-polished Aluminum surfaces while the total reflection is lower than for Aluminum. There are two reasons why we are treating this sample again here. First, in the previous works we did not measure the direct back-scattering and the hemispherical scattering in p-polarization. Thus, we aim for completeness by including these measurements into the whole scattering scheme. Second, we did some minor upgrades to the hemispherical scatterometer since 2017 which decreased the influence of the PD holder on the

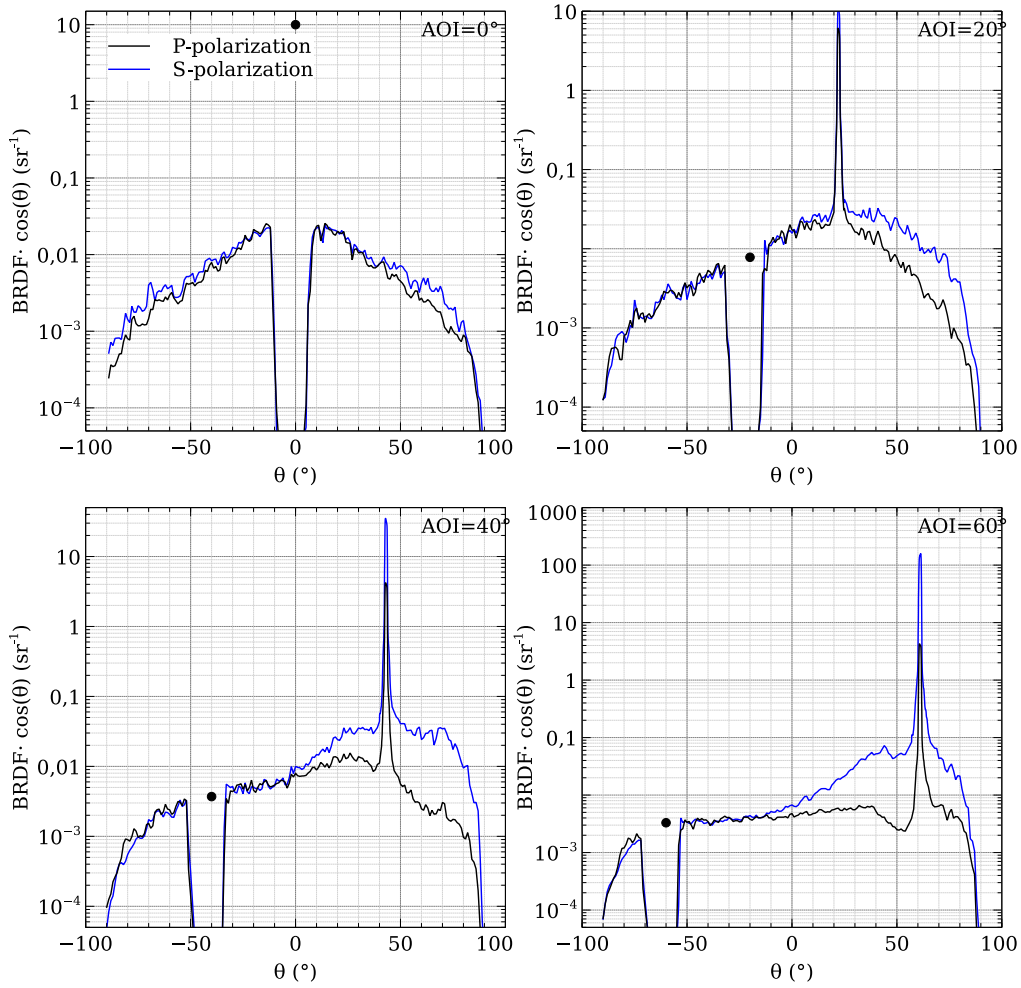


Fig. 6. Scattering probability of the Solblack sample showing the hemispherical scattering along the plane of incidence at 0, 20, 40, and 60°AOI. The black dots mark the results of the back-scattering measurements at the respective AOI.

measured intensities especially around the specular peak. We think that these additional data will give us also more insights regarding the analysis of the scattering curves (please refer to section 4 and especially Fig. 13).

In Fig. 6, the hemispherical scattering curves are shown for four different AOIs (0°, 20°, 40°, and 60°) at two polarizations in a direct comparison. Obviously, the differences between the polarization are increasing with increasing AOI, as one would expect with the approach to the Brewster-angle, which Akutsu et al. [9] found to be around 53°. But not only the overall strength of the BRDF is different, also the specific shape of the hemispherical scattering differs for the two polarizations, very much in contrast to SiC. Especially prominent in the curves is a bulge in s-polarization, symmetrically formed around the specular peak, which does not appear in p-polarization. This bulge is becoming more and more prominent with increasing AOI. Notable is also that there are no visible differences between both polarization for scattering angles below 0°. Calculating the integrated scattering in the same angular range around the specular peak as done for the SiC samples resulted in similar reflectance values as given in Akutsu et al. [9] (see Fig. 8).

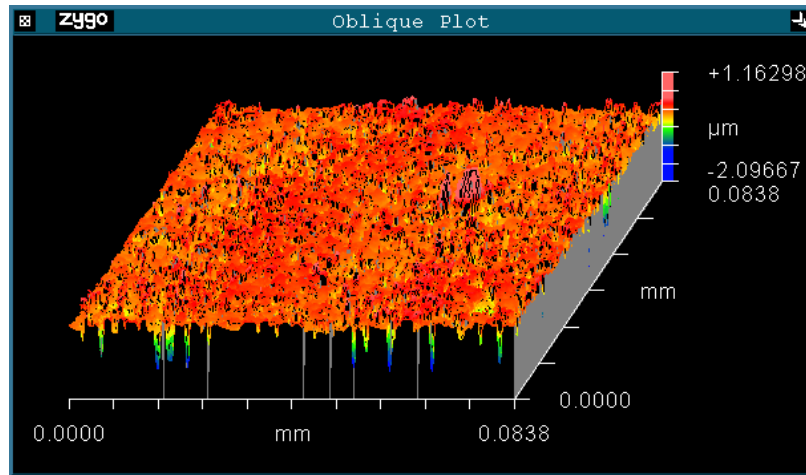


Fig. 7. Surface structure as measured by Zygo’s NewView instrument on a Solblack sample. The surface seems relatively smooth but there are many  $\sim 1\mu\text{m}$  deep, steep structures visible as well.

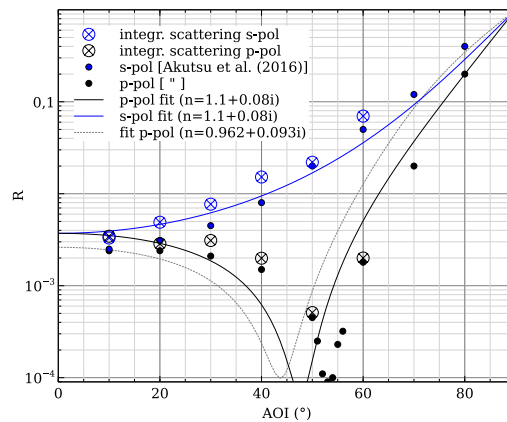


Fig. 8. Reflectance of the Solblack sample: measured (from [9]) and calculated from the scattering data. Additionally, the theoretical reflectance according to the Fresnel-formula is given (for p-polarization from [9], and for s- and p-polarization from the model calculations treated in section 4.2.).

However, taking a much wider angular range (assuming a symmetrical distribution of scattering around the specular peak), the values soon increase a lot toward a total reflectance of  $\sim 3\%$  for small AOIs, which is approximately 10 times higher than the value given in [9]. Given in Fig. 8 are also Fresnel-curves calculated with a refraction index of  $1.1 + 0.08i$ . This value has been estimated according to the model describing the scattering (see also section 4.2.).

In addition to the hemispherical scattering data, the back-scattering probabilities are given as black dots.

### 3.3. “VantaBlack”

Under the name “VantaBlack” a new type of black coating (high absorptive coatings) has been published in 2014 by Surrey NanoSystems© [8]. “Vanta” stands for *Vertical Aligned Nanotube Array* and consists of carbon nanotubes of 20 – 30  $\mu\text{m}$  length which are placed vertically on a

metal surface. This coating is claimed to be the blackest on Earth, and indeed the hemispherical reflectivity of less than 1% in near infrared wavelength ranges is very low [8, 18]. With kind permission of Surrey NanoSystems©, in 2016 we were granted with a sample of a VantaBlack coated Aluminum plate for which we determined the hemispherical scattering in terms of the scattering-probability for 4 different AOIs along the plane of incidence (see Fig. 9). Nowadays, there are more advanced versions of this coating available, but since it is our only sample in this investigation, we will refer to the sample henceforth as VantaBlack.

As can be seen, no specular beam could be found in the scattering for oblique incidence. Also the back-scatterometer was not able to show any hint of a measurable specular reflection (the measured data are dominated by the mentioned background-radiation field and therefore are not shown in the figure). Instead, the scattering is well distributed for normal incidence between  $2 \cdot 10^{-5}$  and  $2 \cdot 10^{-4} \text{ sr}^{-1}$  without any remarkable features but with slight differences between both polarizations. Toward wider AOIs, however, the distribution becomes more and more antisymmetric with respect to the surface's normal for both polarizations and shows a kind of feature for  $60^\circ$  AOI at  $\theta = 82^\circ$ , which measures  $0.003 \text{ sr}^{-1}$  for both polarizations. It is thus a relatively weak feature, compared to the specular peaks of "Solblack" or SiC. While the scattering-probability shows only a growing feature in s-polarization with increasing AOI, a local minimum is visible for the p-polarization. It begins to appear at  $60 - 70^\circ$  longitude when the AOI becomes  $20^\circ$ . It then further shifts toward  $\theta = 0^\circ$  as the AOI increases. The sharp feature at  $40$  and  $60^\circ$  AOI, shortly before the gap of the PD's shadow, is actually an artifact due to an increased reflectance at the edge of the PD holder.

#### 4. Consistency with existing models

Theoretical models for describing the angular scattering became more and more important in recent years. One reason is the need of simple prescriptions creating realistic views of three dimensional computer models. But not only in computer graphics, basically in every field where a proper precipitation of light-scattering is necessary, these models are of great importance. One of these fields is the interferometric gravitational-wave-detector construction. Even weak portions of scattered light which find the way back to the main beam can carry noisy phase information worsening the noise level of the detector [7]. For calculating the sensitivity threshold of such detectors, it is mandatory to have an idea about the amount of scattering light inside the evacuated chambers, hosting the mirrors.

Measurements as those presented in this paper give already an overview of the scattering from a specific material. However, the measured data are not representing the hemispherical scattering as a whole but only along one plane of incidence. A complete hemispherical measurement is also only seldom possible, and not with our apparatus right now (however, such devices exist, as presented, e.g., in [19]). Furthermore, we need to put a physical meaning into measured data. Therefore, in a comprehensive presentation, surface-scattering models like RR (Raileigh-Rice) or GHS (Generalized Harvey-Shack) are needed. These models are relatively simple and easy to apply. Nevertheless, they are also limited to certain constraints. They are basically not suitable for coated surfaces and depend strongly on a (measured or otherwise assumed) PSD as mentioned above, which again has its limitations. The GHS model for smooth surfaces, for example, can be given as [3]:

$$\text{BRDF}_m(\theta_{\text{in}}, \theta_{\text{sc}}, \phi_{\text{sc}}) = \frac{4\pi^2}{\lambda^4} \cdot (\cos \theta_{\text{in}} + \cos \theta_{\text{sc}})^2 \cdot Q \cdot \text{PSD}(f_x, f_y), \quad (3)$$

with

$$f_x = \frac{\sin(\theta_{\text{sc}}) \cos(\phi_{\text{sc}}) - \sin(\theta_{\text{in}})}{\lambda}, \quad f_y = \frac{\sin(\theta_{\text{sc}}) \sin(\phi_{\text{sc}})}{\lambda}, \quad (4)$$

where  $\theta_{\text{in}}$  and  $\theta_{\text{sc}}$  are the AOI and the longitude, respectively, while Q refers to the polarization

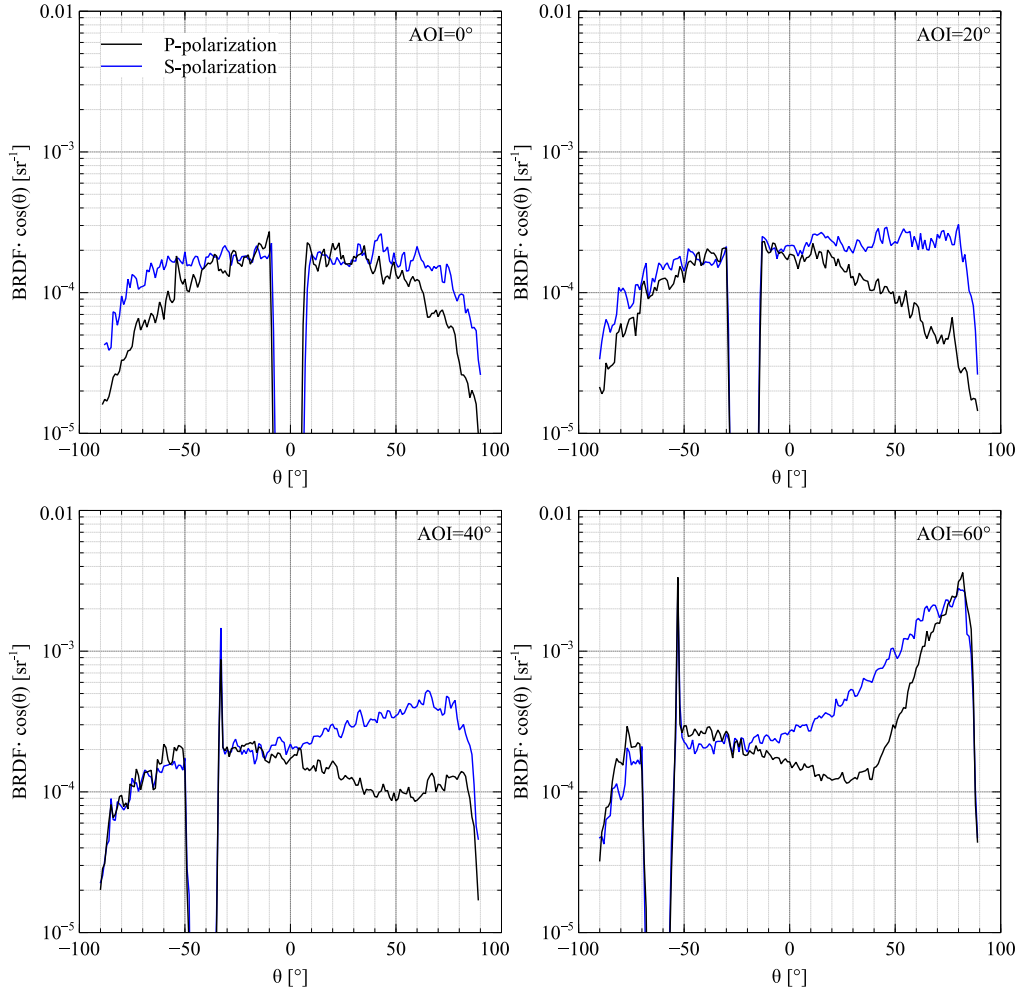


Fig. 9. Scattering probability of the VantaBlack sample showing the hemispherical scattering along the plane of incidence at 0, 20, 40, and 60°AOI.

dependent reflectivity [4] which is also a function of the AOI, the latitude, the longitude  $\phi_{sc}$ , and the dielectric index. The PSD is two-dimensional and a function of the spatial frequencies  $f_x$  and  $f_y$  which are in turn a function of AOI, longitude, and latitude [4].

In this section, we are comparing the measured BRDF data from the samples presented in the previous section with the model given in Eq. (3). The most crucial part thereby is the PSD. From the metrology measurements which are shown in Fig. 3 and 7, we can derive the necessary data. Unfortunately, it is not possible to extract a two-dimensional PSD from Zygo's MetroPro software (vs. 8.1.3), only one-dimensional data can be read-out. However, one can estimate the two-dimensional one with a fit of a one-dimensional PSD. Such a fit is based on the ABC-model [7, 20] and was done with three sets of parameters which are given in table 2. The basic function for a one-dimensional PSD is

$$\text{PSD}_{1-D} = \frac{A}{[1+(Bf)^2]^{C/2}} \quad (5)$$

$$f = \sqrt{f_x^2 + f_y^2}. \quad (6)$$

Then, we use the same fit-parameters  $A$ ,  $B$ , and  $C$  for getting the two-dimensional PSD:

$$\text{PSD}_{2-D} = K \cdot \frac{AB}{[1+(Bf)^2]^{(C+1)/2}} \quad (7)$$

$$K = \frac{1}{2\sqrt{\pi}} \cdot \frac{\Gamma[(C+1)/2]}{\Gamma(C/2)}. \quad (8)$$

$\Gamma$  means here the gamma function. This approach works under the constraint of an isotropic surface roughness which is basically given for the SiC and “Solblack” samples. However, it should be noted that finding suitable PSD data is difficult and results typically in a potpourri of curves which can have differences of 2 orders of magnitude, thus increasing the variance of the BRDF model calculation accordingly. Also, the quality of the extracted PSD data in certain spatial-frequency ranges depends strongly on the zoom-level of the maps which we have taken. Therefore, as a rule of thumb, for those samples where we could take surface-maps at 20x and 100x zoom-level, we used the 20x maps for fitting at frequencies below  $100 \text{ mm}^{-1}$ , and the 100x maps for frequencies above that value. As for “VantaBlack”, a different approach was chosen since we could not measure the surface roughness.

#### 4.1. SiC

In Fig. 11, the results of utilizing the GHS model with the surface-data taken from the SiC samples is given. It shows the hemispherical scattering probability for  $20^\circ$ ,  $40^\circ$ , and  $60^\circ$  AOI, constructed by using PSD data from several spots on each sample’s surface, which are shown in Fig. 10. We think that taking data from different spots is a reasonable approach as we are assuming the sample-surfaces to be isotropic and we were not able to target one and the same spot for every measurement. For the SiC1 sample, we have two different PSD curves: one for a surface map taken at 10x zoom-level and one for a map taken at 100x zoom-level. It turned out that for all PSD curves, the 100x map gives by a factor 5~10 higher values than the 10x map in their overlaying spatial frequency range. As we have more confidence in the data taken from the 10x map in the frequency range  $10 - 150 \text{ mm}^{-1}$ , the fit is oriented to this map, while for higher frequencies it is oriented to the 100x map. Unfortunately, we could not get a good map in the 10x zoom-level for SiC2. Instead, we took PSDs from several spots on the surface with 100x maps (as shown in Fig. 6). Three of those PSD curves are shown in Fig. 10 together with a fit to them. The ABC-parameter from the fits are presented in Table 2. We found that a set of 3 different PSD functions fit best the one-dimensional PSD curves from Fig. 10. The dielectric index, necessary for the Q-factor is  $\varepsilon = 6.33 + 0.71i$ . In addition to that, we assume a Lambertian scattering background.

The modeled BRDF reproduces the measured data quite well, especially the different development of the p- and s-polarization with increasing AOI around the specular reflection peak. This shows that our measurement-setup is sufficiently good in terms of accuracy. The fact that for wide scattering angles ( $\theta < 0^\circ$  in the figure), the scattering probability does not show remarkable differences between the directions of polarization, is the reason why a Lambertian background is being assumed here ( $0.003 \text{ sr}^{-1}$  for SiC1 and  $0.001 \text{ sr}^{-1}$  for SiC2). This is supported by the general (multi-crystalline) structure of SiC, having a lot of deep, hollow structures beneath and on the surface with up to one micrometer in diameter on an otherwise smooth surface (see above sections), giving rise to subsurface scattering which is generally assumed to be diffuse [21]. However, the conformity of the model with the measured data for wide scattering angles in all

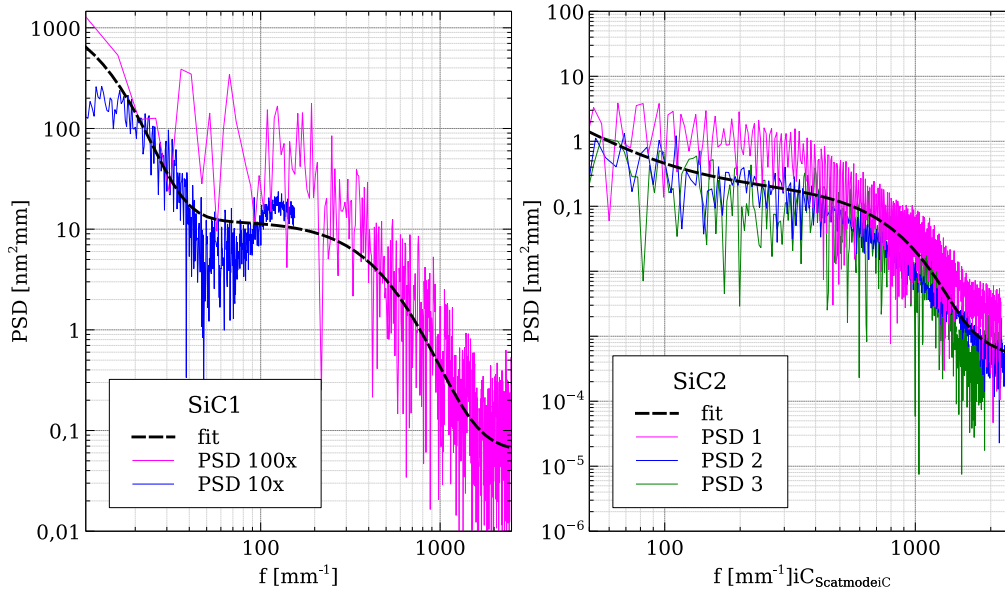


Fig. 10. PSD data (one-dimensional) taken from the surface maps with the aid of Zygo's MetroPro software for both SiC samples and the fits calculated according to those data.

AOIs is basically better for the SiC2 sample. For SiC1 it seems that at wider AOIs the scattering is decreasing a bit, especially in s-polarization.

Table 2. Parameters used for the ABC-model to fit the measured PSD of the SiC2 sample.

		$A$	$B$	$C$
		$[\text{nm}^2\text{mm}]$	$[\text{mm}]$	
SiC1	Set 1	1500	0.05	7
	Set 2	12	0.0016	5.5
	Set 3	0.07	0.13	0.02
SiC2	Set 1	1530	262.942	1.15
	Set 2	931.7	0.4	2.23
	Set 3	0.2	0.0002	122.76

#### 4.2. "Solblack"

As it has been shown already in [9], the scattering distributions for Solblack (in s-polarization) can be well approximated with a Lorentzian for the diffuse scattering at small AOIs and the specular reflection peak (all along the POI). As the incident angle is increasing, however, the scattering toward wide scattering-angles differs more and more from a Lorentzian curve. Also, due to its behavior with the approach to the Brewster-angle, the p-polarization curve seems to be even less describable with such a function (see Fig. 6).

In Fig. 13, the results of the calculated scattering probability compared with the data from the measurements are shown for three AOIs (20°, 40°, and 60°) in both polarizations. The (one-dimensional) PSD has been calculated as a fit to data taken again from the surface maps as shown already for SiC. The PSD data and the respective fit can be found in Fig. 12. As it was the case for SiC2, we took maps at a 100x zoom-level and calculated the fit to a mean of several PSD-curves. The fit-parameters are given in table 3.

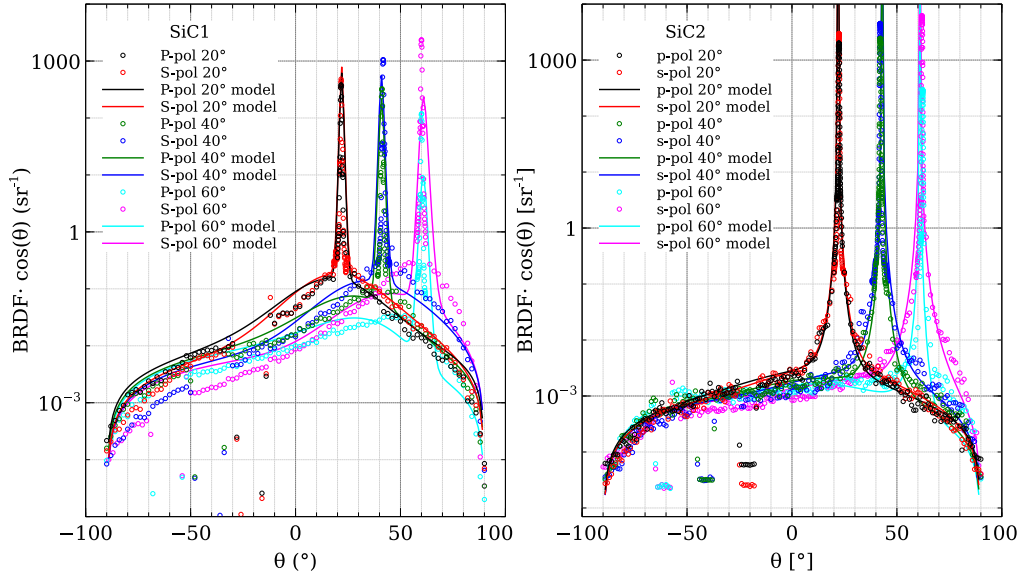


Fig. 11. Comparison of the scattering probability both measured and calculated (see text) for SiC. The graph includes the data for three different AOIs at s- and p-polarization.

As can be seen, the shape of the calculated scattering curves matches relatively well with the measured data. However, it should be noted that we have used here a more general form of the parameter  $Q$  according to [22, 23], which is a function of the dielectric index  $\varepsilon$  and the relative magnetic permeability  $\mu$ , as NiP-plating's magnetism is generally depending on the Phosphor content [24]. However, we found that still  $\mu \approx 1$  fits best the curves. As a considerable diamagnetism is not reported for these plating, we set  $\mu = 1$  for the curves shown in Fig. 13. The dielectric index, on the other side, was found to be  $\varepsilon \approx 1.2 + 0.176i$ . That corresponds to a refraction index of  $n = 1.1 + 0.08i$  which is somewhat comparable to the integrated scattering calculations and the measurements done by Akutsu et al. [9] (see Fig. 8). The real part of the dielectric index is anyway quite low but considering the above mentioned fractal and porous structure, the resulting dielectric index of the actual coating material can be explained by effective-medium theory. Indeed, past studies on the optical properties of NiP coatings support this assumption [25].

Table 3. Parameters used for the ABC-model to fit the measured PSD of the Solblack sample.

	$A$	$B$	$C$
	[nm <sup>2</sup> mm]	[mm]	
Set 1	180.1	0.0014	6.2
Set 2	157	0.0652	4.32
Set 3	0.55	2.0411	0.05

As Solblack is a coating one would assume that a single-surface scattering theory may be not usable. However, according to our reflection measurements and the fits, the imaginary part of the index of refraction is  $\geq 0.08$  and thus the linear absorption coefficient is too large to let any significant amount of light-power pass through the Solblack coating.

As it is the case for SiC, also for Solblack we have used an additional Lambertian scattering component to gain consistency with the measured data. It is approximately 3 times higher than for the SiC2 model and thus similar to SiC1. We assume that the mentioned random inhomogeneous

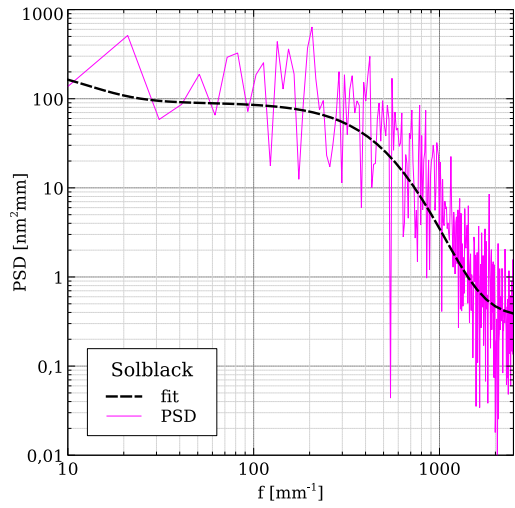


Fig. 12. PSD data (one-dimensional) taken from the surface maps with the aid of Zygo's MetroPro software for the Solblack sample and the fit calculated according to the data.

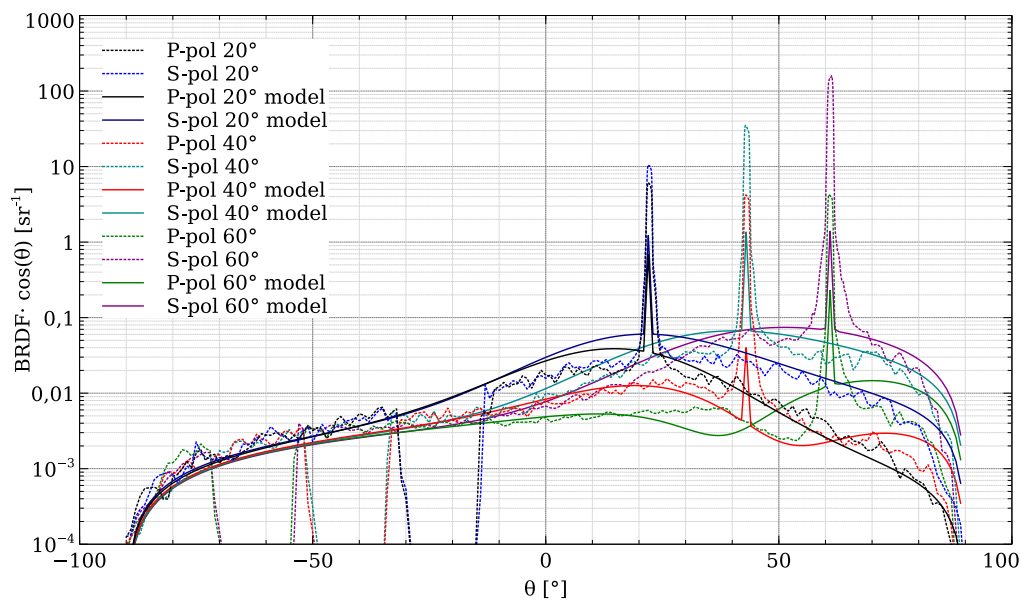


Fig. 13. Comparison of the scattering probability both measured and calculated (see text) for Solblack. The graph includes the data for three different AOIs at s- and p-polarization.

structures may be one of the reasons for a diffuse scattering component. Moreover, as the absorption index of Solblack is also lower than that for SiC and consequently more light is available for subsurface scattering (as introduced, e.g., in [21]), an increased Lambertian component seems to be reasonable.

### 4.3. "VantaBlack"

The surface structure of VantaBlack is featured by carbon nanotubes having a diameter of only a few nanometers. These densely aligned tubes would not show any remarkable feature of the

corresponding surface PSD until  $f_{x,y} \approx 10^4 - 10^5 \text{ mm}^{-1}$ , which is far too high a spatial frequency for being recognized by near-infrared light. At the same time, it seems that the multitude of tips of carbon nanotubes, which are supposed to mimic the surface structure of the substrate, are not reflecting any reasonable amount of light directly back into the surrounding medium. Instead, most of the (near infrared) light is being absorbed and the rest diffusely scattered.

Surface scattering theories predict homogeneous scattering as observed for VantaBlack only by completely random surface structures. However, the VantaBlack sample may not have a random surface as for mentioned reasons. But considering the nanotubes as hollow cylinders with very thin walls, it seems reasonable to assume that the PSD of the original substrate-surface is quasi suppressed especially for lower spatial frequencies as the light is entering the cylinders and being absorbed or trapped rather than being reflected. This may lead to a quasi-randomized surface for lower spatial frequencies. Therefore, as a first approach, we assume a constant PSD over the whole relevant range of spatial frequencies and try to fit the experimental results with a GHS-model, giving us an expression for a perfectly random surface-structure. Unfortunately, it was not possible to proof our assumption of a quasi-constant PSD as the metrology measurements that we can perform in our institute would not work with such highly absorptive surfaces. Anyway, ABC-parameters for a quasi-PSD calculation according to our assumptions are given in table 4.

Table 4. Parameters used for the quasi-constant ABC-model of the VantaBlack sample.

A	B	C
[nm <sup>2</sup> mm]	[mm]	
3000	10 <sup>-6</sup>	1.5

For a calculation of the scattering, we also need the refraction index of the material. But as we have no measurable specular reflection peak, it is impossible for us to undertake the procedure that has been used for SiC and Solblack. However, past studies have shown that it is possible to define an effective dielectric index for alignments of carbon nanotubes from the dielectric index of graphite layers [26, 27]. According to their model, the material has an inhomogeneous dielectric index with respect to the orientation of the incoming electromagnetic wave toward the nanotubes. Hence, we have to deal with basically two different dielectric indexes: an index for fields perpendicular to the tubes and an index for fields parallel to them. As a consequence, s-polarization represents now the fields perpendicular to the tubes while p-polarization can be perpendicular and parallel to the tubes, depending on the AOI. Measurements on the permeability have shown that the index is actually very much depending on impurities due to the used catalyst material. For pure Carbon nanotubes, however, it should be diamagnetic ( $\mu < 1$ ) [28].

Anyway, the best fit to our measurements for AOI = 0° was found with  $\mu = 1.15$  and an effective dielectric index  $\epsilon_{\text{eff}} = 1.26 + 0.235i$ . With increasing AOI, we found that  $\epsilon_{\text{eff}}$  in s- and p-polarization should slightly decrease to be more consistent with the measurements. The values for  $\epsilon_{\text{eff}}$  are given in table 5.

Table 5. Dielectric index  $\epsilon_{\text{eff}}$  used to fit the scattering probability curves of the VantaBlack sample.

AOI	0°	20°	40°	60°
s-polarization	1.26 + 0.235i	1.24 + 0.235i	1.2 + 0.235i	1.17 + 0.217i
p-polarization	1.26 + 0.235i	1.13 + 0.226i	1.1 + 0.209i	1.12 + 0.219i

The result of the calculations can be seen in Fig. 14 showing the scattering probability for 3 different AOIs. The basic shape and its development with increasing AOI can be well simulated for AOI  $\leq 40^\circ$  with the given parameters. However, toward AOI  $\approx 60^\circ$  our model is not able

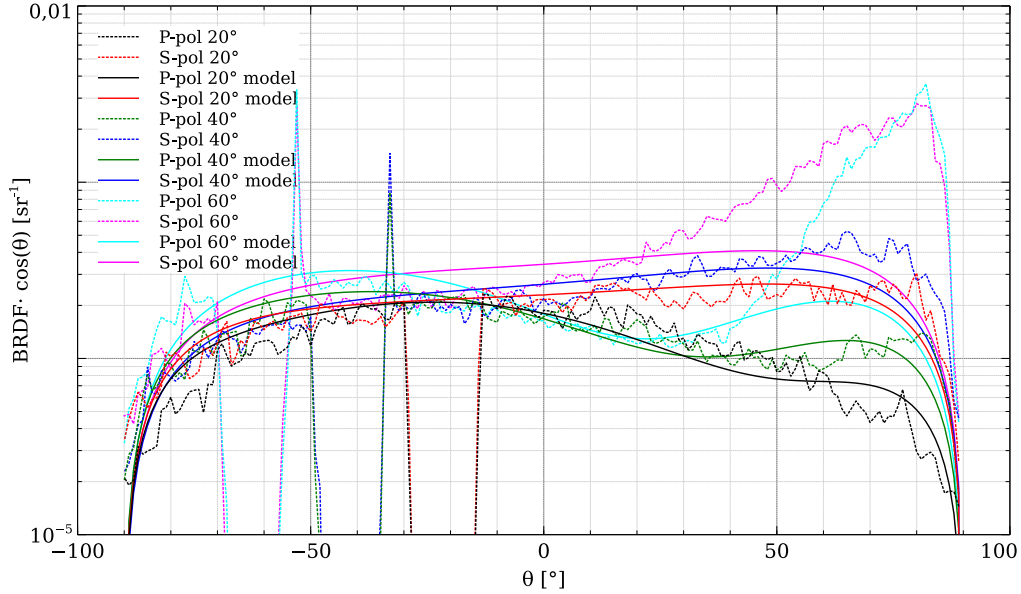


Fig. 14. Comparison of the scattering probability both measured and calculated (see text) for VantaBlack. The graph includes the data for three different AOIs at s- and p-polarization.

to increase the scattering enough for the bulge at  $\theta \approx 80^\circ$ . This is in particular true for the p-polarization. In s-polarization there is also an inconsistency with the measurements for  $\theta \leq 0^\circ$  where the model predicts a slightly higher scattering than observed.

The results seem to be somewhat consistent with the findings of [26] for densely aligned carbon nanotubes with small inner radius, leading to values of  $\epsilon_{\text{eff}}$  being  $\leq 1.5$  in its real and  $\leq 1$  in its imaginary part. Tubes having a small inner radius would be also consistent with our assumption of a suppressed low-frequency PSD. One should note, however, that in [26], the authors do not present parameters for all possible cases and hence their  $\epsilon_{\text{eff}}$  does not exactly cover our findings. But we think that our results are not unreasonable and lie in the overall tendency presented in their spectra.

## 5. Discussion/Conclusion

With our scatterometers we have done measurements on various surfaces from different materials being related to gravitational-wave detectors for suppressing stray-light. We used the results from three of the most important materials as a basic example in this paper to show the functionality of these scatterometers. We have shown their capabilities both in terms of contrast and spatial resolution over the whole hemisphere along the plane of incidence (POI) of a given surface. Right now, the hemispherical scatterometer has a higher sensitivity compared to the back-scatterometer which is an issue for surfaces with very low scattering as we cannot get reliable data on their back-scattering (as it was the case for the VantaBlack sample). All measurements were done under similar environmental conditions and showed a sufficient repeatability (for each presented sample, we did 2 – 3 measurement runs showing maximal deviations of  $\lesssim 10\%$  which is within an acceptable range.) Furthermore, we were able to reproduce the measured results with a scattering model to a certain extend and could estimate the properties of the respective material, which are (in case of SiC and Solblack) comparable to data taken from reflection measurements. We could show that for a proper reproduction, it is in some cases important to include the magnetic properties in the respective models, even though they are relatively small. We would like to

emphasize that the presented measurements and our approach for an interpretation is new to the field of gravitational-waves and may be of great usage for future detectors.

Nevertheless, there are still discrepancies regarding the models and the measurements. Still unclear, for example, is the relatively large scattering bulge for VantaBlack at  $\theta \sim 80^\circ$  for  $60^\circ$  AOI in both s- and p-polarization. Even with further increase of the dielectric index or the magnetic permeability, the corresponding model would not show such a strong bulge. Considering the simpleness of our approach, it is very likely that a more comprehensive PSD assumption (based on, e.g., atomic-force microscopy measurements) or even a different model may have more success in an explanation. Therefore, a follow-up investigation on this issue would be appreciated. However, we think that finding a permeability being higher than 1 is anyway very interesting and can indicate a possible impurity of the nanotubes.

There are also discrepancies with the Solblack measurements but they are smaller and likely due to an inaccurate PSD. However, generally, the used model is successful in representing the measured data for both SiC and Solblack, and for VantaBlack at small AOIs.

There are some points noteworthy:

1. The assumed index of refraction is in case of SiC based on Fresnel-fits to measured reflectance-data from a highly polished sample (SiC2) as we can be sure that the scattering from the roughly polished sample (SiC1) is limited in its accuracy. Since we don't have such a highly polished sample for Solblack (which is also not existing, to our knowledge), we cannot be sure about the index of refraction from reflectance measurements and hence, our approach is a little bit different. We adjusted the index of refraction to the scattering data with the model from Eq. (3) and the parameter Q as given in [22].
2. Due to the variance of PSD data from the surface maps, it is generally difficult to be sure about the absolute value of the scattering when we compare our measurements with the given model. Therefore, our main focus laid rather on the representation of the general shape of the scattering curves.
3. Even though the measured roughness of the samples is in a range where a smooth-surface approach (with the given GHS model) is reasonable, especially the SiC1 and the Solblack sample might partly violate this assumption, which gives rise to an additional uncertainty regarding the calculated scattering models. This, in turn, would also affect the made assumptions regarding the PSD and the refractive index. Our approach is thus just a suggestion of how the data may be interpreted.

It should be also noted that we are planning to upgrade the devices further and to make them clean-room or even vacuum compatible. For instance, the light-trap which we are using for the back-scatterometer should therefore not be coated with soot.

We have seen that from all three materials the scattering properties of VantaBlack are most outstanding, especially compared to Solblack, which is used in many subsystems of KAGRA. However, its usability in tough environments like (ground-based) gravitational wave detectors remains somewhat limited. It is more easy to remove from its substrate when touching it, and also its outgassing-rate is 4 times higher than that of Solblack (after 2 days in vacuum, the outgassing rate for VantaBlack on a plate of Aluminum is  $\sim 4 \cdot 10^{-6} \text{ Pa}\cdot\text{m}^3\cdot\text{s}^{-1}\cdot\text{m}^{-2}$ , while for Solblack on Aluminum it is  $\sim 10^{-6}$  [9]). Nevertheless, VantaBlack has the possibility to become an important scattering suppressing coating in future gravitational wave detectors, as we are sure that with a further increasing sensitivity, the issue of scattering may increase as well.

## **Acknowledgements**

This work was supported by MEXT, JSPS Leading-edge Research Infrastructure Program, JSPS Grant-in-Aid for Specially Promoted Research 26000005, JSPS Grant-in-Aid for Scientific Research on Innovative Areas 2905: JP17H06358, JP17H06361 and JP17H06364, JSPS Core-to-Core Program A. Advanced Research Networks, JSPS Grant-in-Aid for Scientific Research (S) 17H06133, the joint research program of the Institute for Cosmic Ray Research, University of Tokyo, National Research Foundation (NRF) and Computing Infrastructure Project of KISTI-GSDC in Korea, the LIGO project, and the Virgo project.